Modelling and Control of TCV

Atul S. Sharma*, David J.N. Limebeer*, Imad M. Jaimoukha*, Jonathan B. Lister+

***Abstract*—A new approach to the modelling and control of tokamak fusion reactors is presented. A nonlinear model is derived using the classical arguments of Hamiltonian mechanics and a low-order linear model is derived from it. The modelling process used here addresses flux and energy conservation issues explicitly and self-consistently. The model is of particular value, because it shows clearly the relationship between the initial modelling assumptions and the resulting predictions. The mechanisms behind the creation of uncontrollable modes in tokamak models are discussed. A normalised coprime factorisation $\mathcal{H}_\infty$ controller is developed for the TCV tokamak[1] using a linearised version of the model, which has been extensively verified on the TCV and JT-60U[2] tokamaks. Recent theory is applied to reduce the controller order significantly whilst guaranteeing *a priori* bounds on the robust stability and performance. The controller is shown to track successfully reference signals that dictate the plasma's shape, position and current. The tests used to verify this were carried out on linear and nonlinear models.**

***Index Terms*—control systems, $\mathcal{H}_\infty$ control, model reduction.**

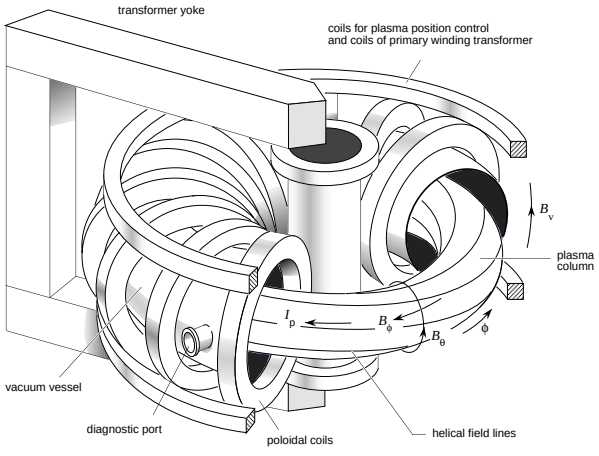

Fig. 1. A diagram of a typical tokamak. Note that the TCV tokamak does not have an iron core (transformer yoke), and has eighteen poloidal field (PF) coils for position and shape control.

I. Introduction

The tokamak was conceived by the Russian scientists Tamm and Sakharov, winners of the Nobel Physics and Peace Prizes respectively. A tokamak[3] is a toroidal device (see Figure 1) that uses magnetic fields to confine a similarly shaped, hot plasma (typically up to 10^8K). This method of confinement exploits the fact that plasmas are made up of free electrons and ions. As a result the plasma can be confined using electromagnetic forces generated by external fields. This external magnetic field has two components. The large toroidal field is produced by a set of poloidally wound coils equally spaced around the vacuum vessel and the smaller poloidal field comes from the induced plasma current. The resultant field is helical as shown schematically in Figure 1.

As a source of power, nuclear fusion has a number of attractive features. The fuels are abundant, there are no long-lived radioactive isotopes produced and it is inherently safe. Nuclear fusion does not contribute to the emission of gases causing the greenhouse effect, or acid rain. At the time of writing, the tokamak is the most promising route to a viable fusion reactor.

The basic characteristics of tokamak equilibria, as described by the Grad-Shafranov equation, are well understood [1] and the theory is relatively accessible [2]. In order to model the gross dynamic behaviour it is possible to make a number of approximations that are accurate enough to provide a basis for robust controller design. A number of linearised models suitable for control system design have already been developed. In the case of the CREATE-L we refer the reader to [3]. Broadly comparable studies have been performed on DIII-D[4] [4], [5], and on TCV [6], [7].

Our modelling research is motivated by the facts that improved models will both further our physical understanding and lead to control systems that extend the operating regimes of existing and future tokamaks such as ITER.

We present a lumped-parameter model that is derived using the established processes of classical Hamiltonian mechanics. For the purposes of model-based controller design, this model can be linearised about any prescribed equilibrium state. As compared with the current art, this model has several distinct features. To begin, flux and energy conservation issues are treated explicitly and self-consistently. In [3], for instance, plasma profile parameters are considered as disturbances, which the authors acknowledge is not self-consistent. Previous derivations of the RZIP-type models [6] have also not considered conservation laws in a self-consistent manner. The consistency issue was first addressed in our previous work [8], where a Lagrangian approach to tokamak modelling was introduced. The derivation presented here results in a linear model similar to those presented in [6] and [8]. This generalised class of lumped-parameter models have been extensively validated against the open-loop response of TCV [6] and the larger, hotter JT-60U machine [8]. An earlier, musch simpler lumped-parameter model describing only the vertical motion of

*Department of Electrical and Electronic Engineering, Imperial College of Science, Technology and Medicine, Exhibition Road, London SW7 2BT, United Kingdom.

+Centre de Recherches en Physique des Plasmas, École Polytechnique Fédérale de Lausanne, Association EURATOM-Suisse, 1015 Lausanne, Switzerland.

[1] at the CRPP-EPFL in Lausanne, Switzerland.

[2] at JAERI in, Naka, Japan

[3] from the Russian '*toroidalnaya kamera magnitnaya katushka*', literally 'toroidal chamber, magnetic coils'

[4] at the General Atomics National Fusion Facility in San Diego, USA

the plasma using an eigenmode description of the passive structures, was validated on DIII-D [9]. Evidence for shortcomings of the RZIP approach exist only for very triangulated plasmas [7], in which case the deformability of the plasma may play a role. However, in the case of the linearised model, a parametric modelling approach can overcome this limitation [8].

We believe that the modelling theory we present here is of particular value, because it shows clearly the relationship between the initial assumptions and the final model. For instance, it becomes obvious that the adiabatic approximation is a natural result of assuming a massless plasma. The next generation of tokamaks will operate on longer time-scales, where plasma resistance effects will become important. Following from [6] and [8], the model presented in this paper considers fully the effects of plasma resistance, showing how to incorporate resistance and mass into the model from the initial stages, if required. The known necessity of current ramping is clearly explained in terms of plasma resistance, as is the creation of uncontrollable modes when a superconducting plasma is assumed. Also, it becomes clear why the use of flux coordinates becomes problematic when plasma resistance is introduced.

A mixed PID-$\mathcal{H}_\infty$ controller has already been designed for COMPASS-D [10] and this methodology was developed and then successfully implemented on TCV [11]. The control scheme was based on the CREATE-L model presented in [3]. In [12], a multi-variable normalised coprime factor $\mathcal{H}_\infty$ controller is designed using a simple single-filament model of the DIII-D tokamak.

High-order $\mathcal{H}_\infty$ controllers can present their own implementation problems. The usual approach is to design the $\mathcal{H}_\infty$ controller about a reduced-order model. In the present paper we develop a reduced-order normalised coprime factor controller for TCV that exploits results presented in [13]. We show that this controller extends the performance of the existing PID schemes [7] and [14]. This approach guarantees both the stability of the closed-loop (via an *a priori* bound condition) and the closed-loop performance via an *a priori* performance bound [13].

In this paper we apply the theory in [13] to the full $\mathcal{H}_\infty$ controller developed for TCV, reducing the controller order from 76 to 18 without a significant loss of performance or robustness. Successful closed-loop tests are performed with the PROTEUS nonlinear tokamak simulation code. The remaining verification step will involve hardware tests on the TCV machine itself.

II. A Hamiltonian Tokamak Model

The aim of this section is to develop a dynamic model of the tokamak using established arguments from Hamiltonian mechanics [15]. The development builds on from that given in [8]. The main components of the model are the poloidal field coils, the passive structure, which carries eddy currents, and the plasma. The poloidal field coils are driven by external voltage sources, while the eddy currents in the passive structure are electromagnetically induced. A cylindrical coordinate system is used, with R the radial coordinate, z the vertical coordinate and ϕ the angular coordinate describing rotation around the z-axis (see Figure 2). When deriving the model, we will make the following assumptions:

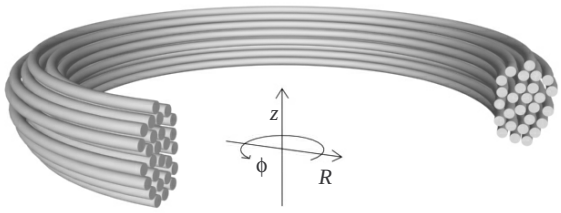

Fig. 2. The plasma is represented by a number of current-carrying elements. The cylindrical coordinate system ($R,\ z,\ \phi$) is shown.

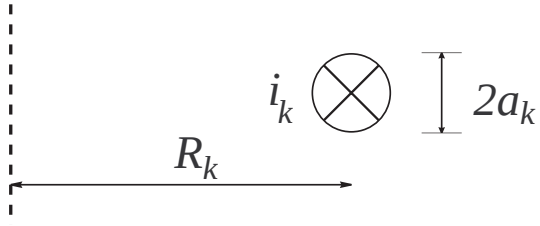

Fig. 3. A plasma current element

- The system is symmetric around the z-axis (axisymmetry);
- Poloidal currents are ignored;
- The tokamak structure will be represented by a finite set of toroidal circuits. We also assume that:
  - These circuits are fixed in space and have finite resistance;
  - The toroidal currents in the structure may vary in time;
- The plasma is represented by a finite number of axisymmetric current carrying elements that have a circular cross-section (see Figure 2). In addition, the filaments will each:
  - carry current that may be time varying;
  - be free to move axisymmetrically;
  - have finite mass and resistance that are assumed constant.

A. The energy functions

In the next phase of the modelling process we will select the generalised coordinates and introduce external voltages into the potential energy function.

Consistent with the modelling assumptions, we define the

generalised coordinates $\boldsymbol{q}$ via

$$\dot{\boldsymbol{q}} = \begin{bmatrix} \boldsymbol{I}_e \\ \boldsymbol{I}_s \\ \dot{\boldsymbol{r}} \end{bmatrix}.$$

The vector $\boldsymbol{I}_e$ contains the currents in the plasma elements, $\boldsymbol{I}_s$ is a vector of structure currents and $\boldsymbol{r} = \begin{bmatrix} \boldsymbol{R} \\ \boldsymbol{z} \end{bmatrix}$ is a vector of position coordinates associated with the plasma current elements.

Next, we introduce the inductance-mass matrix:

$$\mathbf{T}(\boldsymbol{q}) = \begin{bmatrix} \mathbf{L}_e & \mathbf{M}_{es} & 0 \\ \mathbf{M}'_{es} & \mathbf{L}_s & 0 \\ 0 & 0 & \mathbf{m}_e \end{bmatrix}$$

in which the $\mathbf{L}$s and $\mathbf{M}$s are the self and mutual inductance matrices. Again, subscript e denotes the plasma elements and subscript s denotes the structure elements. The matrices $\mathbf{L}_e$ and $\mathbf{M}_{es}$ are functions of plasma element position, because the plasma current elements are free to move axisymmetrically. The structure self-inductance matrix, $\mathbf{L}_s$, is constant. Note that $\mathbf{M}_{se} = \mathbf{M}'_{es}$. The constant diagonal mass matrix, $\mathbf{m}_e$, contains the mass of each plasma current element.

The input vector is given by:

$$\boldsymbol{U} = \begin{bmatrix} \boldsymbol{V}_e \\ \boldsymbol{V}_s \\ 0 \end{bmatrix}$$

where $\boldsymbol{V}_e$ is a vector of effective voltages applied to each plasma element (for example by ion injection) and $\boldsymbol{V}_s$ is the vector of externally applied poloidal field coil voltages.

The resistance matrix is defined as

$$\boldsymbol{\Omega} = \begin{bmatrix} \boldsymbol{\Omega}_e & 0 & 0 \\ 0 & \boldsymbol{\Omega}_s & 0 \\ 0 & 0 & 0 \end{bmatrix}.$$

The generalised kinetic energy is given by:

$$\mathcal{T} = \frac{1}{2}\dot{\boldsymbol{q}}'\mathbf{T}\dot{\boldsymbol{q}} \tag{1}$$

and the generalised potential energy is:

$$\mathcal{V} = -W - \boldsymbol{q}'\boldsymbol{U} + \frac{1}{2}\frac{\mathrm{d}\left(\int_{\boldsymbol{q}(t_0)}^{\boldsymbol{q}(t)}\int_{\boldsymbol{q}(t_0)}^{\boldsymbol{q}(t)}\mathrm{d}\boldsymbol{q}'\boldsymbol{\Omega}\mathrm{d}\boldsymbol{q}\right)}{\mathrm{d}t}, \tag{2}$$

in which W represents the plasma's internal energy.

As usual, the Lagrangian is given by:

$$\mathcal{L} = \frac{1}{2}\dot{\boldsymbol{q}}'\mathbf{T}\dot{\boldsymbol{q}} + W + \boldsymbol{q}'\boldsymbol{U} - \frac{1}{2}\frac{\mathrm{d}\left(\int_{\boldsymbol{q}(t_0)}^{\boldsymbol{q}(t)}\int_{\boldsymbol{q}(t_0)}^{\boldsymbol{q}(t)}\mathrm{d}\boldsymbol{q}'\boldsymbol{\Omega}\mathrm{d}\boldsymbol{q}\right)}{\mathrm{d}t}. \tag{3}$$

The term containing $\boldsymbol{\Omega}$ is the total energy dissipated from time t_0 to t; it is essentially an integral form of Ohm's law. In the Hamiltonian formulation, the dissipation term must be included in $\mathcal{V}$ and not as a separate power dissipation function.

B. The plasma internal energy

We will see later that the internal energy W varies as $\boldsymbol{R}\boldsymbol{I}_e^2$. As such, we can express it as

$$W = \frac{\boldsymbol{q}'\mathbf{E}\dot{\boldsymbol{q}}^2}{2} \tag{4}$$

where $\mathbf{E}$ is a constant matrix. The $\dot{\boldsymbol{q}}^2$ notation refers to a vector containing quadratic terms in each entry (the elemental currents in this case).

This representation is chosen for convenience when forming the Hamiltonian.

C. The Equations of Motion

Using the above we can now express the Lagrangian (3) as

$$\begin{aligned}\mathcal{L} =& \frac{1}{2}\dot{\boldsymbol{q}}'\mathbf{T}\dot{\boldsymbol{q}} + \frac{\boldsymbol{q}'\mathbf{E}\dot{\boldsymbol{q}}^2}{2} + \boldsymbol{q}'\boldsymbol{U} \\ & - \frac{1}{2}\frac{\mathrm{d}\left(\int_{\boldsymbol{q}(t_0)}^{\boldsymbol{q}(t)}\int_{\boldsymbol{q}(t_0)}^{\boldsymbol{q}(t)}\mathrm{d}\boldsymbol{q}'\boldsymbol{\Omega}\mathrm{d}\boldsymbol{q}\right)}{\mathrm{d}t}.\end{aligned} \tag{5}$$

To form the Hamiltonian, via the correct Legendre transformation, the generalised momenta are computed next:

$$\boldsymbol{p} = \frac{\partial\mathcal{L}}{\partial\dot{\boldsymbol{q}}}$$

giving

$$\boldsymbol{p} = \mathbf{T}\dot{\boldsymbol{q}} + \boldsymbol{q}'\mathbf{E}\dot{\boldsymbol{q}}. \tag{6}$$

The Hamiltonian is given by

$$\mathcal{H} = \boldsymbol{p}'\dot{\boldsymbol{q}} - \mathcal{L}$$

or equivalently:

$$\begin{aligned}\mathcal{H} =& \frac{1}{2}\dot{\boldsymbol{q}}'\mathbf{T}\dot{\boldsymbol{q}} + \frac{1}{2}\boldsymbol{q}'\mathbf{E}\dot{\boldsymbol{q}}^2 - \boldsymbol{q}'\mathbf{U} \\ & + \frac{1}{2}\frac{\mathrm{d}\left(\int_{\boldsymbol{q}(t_0)}^{\boldsymbol{q}(t)}\int_{\boldsymbol{q}(t_0)}^{\boldsymbol{q}(t)}\mathrm{d}\boldsymbol{q}'\boldsymbol{\Omega}\mathrm{d}\boldsymbol{q}\right)}{\mathrm{d}t}.\end{aligned} \tag{7}$$

We now eliminate $\dot{\boldsymbol{q}}$ using (6), to obtain the Hamiltonian in terms of $\boldsymbol{p}$, $\boldsymbol{q}$ and t:

$$\begin{aligned}\mathcal{H}(\boldsymbol{p},\boldsymbol{q},t) =& \frac{1}{2}\boldsymbol{p}'\left[\mathbf{T}+\boldsymbol{q}\mathbf{E}\right]^{-1}\boldsymbol{p} - \boldsymbol{q}'\boldsymbol{U} \\ & + \frac{1}{2}\frac{\mathrm{d}\left(\int_{\boldsymbol{q}(t_0)}^{\boldsymbol{q}(t)}\int_{\boldsymbol{q}(t_0)}^{\boldsymbol{q}(t)}\mathrm{d}\boldsymbol{q}'\boldsymbol{\Omega}\mathrm{d}\boldsymbol{q}\right)}{\mathrm{d}t}.\end{aligned} \tag{8}$$

The relation

$$\dot{\boldsymbol{p}} = -\frac{\partial\mathcal{H}}{\partial\boldsymbol{q}} \tag{9}$$

gives

$$\begin{aligned}\frac{\mathrm{d}\left(\mathbf{T}\dot{\boldsymbol{q}} + \boldsymbol{q}'\mathbf{E}\dot{\boldsymbol{q}} + \boldsymbol{\Omega}\boldsymbol{q}\right)}{\mathrm{d}t} =& \boldsymbol{U} + \frac{\mathbf{E}\dot{\boldsymbol{q}}^2}{2} + \frac{1}{2}\dot{\boldsymbol{q}}'\frac{\partial\mathbf{T}}{\partial\boldsymbol{q}}\dot{\boldsymbol{q}} \\ & - \frac{1}{2}\frac{\mathrm{d}\left(\int_{\boldsymbol{q}(t_0)}^{\boldsymbol{q}(t)}\mathrm{d}\boldsymbol{q}'\boldsymbol{\Omega}\right)}{\mathrm{d}t},\end{aligned} \tag{10}$$

which is the required equation of motion.

This equation can now be expanded into four vector equations. The equation for $\boldsymbol{I}_e$ is:

$$\frac{\mathrm{d}\left(\mathbf{L}_e\boldsymbol{I}_e+\mathbf{M}_{es}\boldsymbol{I}_s+\boldsymbol{R}\mathbf{E}\boldsymbol{I}_e\right)}{\mathrm{d}t}+\boldsymbol{\Omega}_e\boldsymbol{I}_e=\boldsymbol{V}_e, \qquad (11)$$

which is essentially a statement of Kirchoff's voltage law for the plasma elements.

Similarly, we have Kirchoff's voltage law for the structural and poloidal circuits, giving the equation for $\boldsymbol{I}_s$:

$$\frac{\mathrm{d}\left(\mathbf{L}_s\boldsymbol{I}_s+\mathbf{M}_{se}\boldsymbol{I}_e\right)}{\mathrm{d}t}+\boldsymbol{\Omega}_s\boldsymbol{I}_s=\boldsymbol{V}_s. \qquad (12)$$

The remaining equations are force balances in the R and z-directions respectively. For $\boldsymbol{R}$ we have:

$$\frac{\mathrm{d}\left(\mathbf{m}_e\dot{\boldsymbol{R}}\right)}{\mathrm{d}t}=\frac{1}{2}\boldsymbol{I}'_e\frac{\partial\mathbf{L}_e}{\partial\boldsymbol{R}}\boldsymbol{I}_e+\boldsymbol{I}'_s\frac{\partial\mathbf{M}_{se}}{\partial\boldsymbol{R}}\boldsymbol{I}_e+\frac{\mathbf{E}\boldsymbol{I}_e^2}{2} \qquad (13)$$

and for $\boldsymbol{z}$:

$$\frac{\mathrm{d}\left(\mathbf{m}_e\dot{\boldsymbol{z}}\right)}{\mathrm{d}t}=\frac{1}{2}\boldsymbol{I}'_e\frac{\partial\mathbf{L}_e}{\partial\boldsymbol{z}}\boldsymbol{I}_e+\boldsymbol{I}'_s\frac{\partial\mathbf{M}_{se}}{\partial\boldsymbol{z}}\boldsymbol{I}_e. \qquad (14)$$

We conclude this section with a number of observations:

- In the case that $\mathcal{H}$ is independent of a particular coordinate, the corresponding canonical momentum will be conserved (see (9), and by Noether's theorem, see [15], Section 12-7). In the same way, if $\mathcal{H}$ is time invariant, the associated system is conservative.
- If $\boldsymbol{U}$ and $\boldsymbol{\Omega}$ are both zero, the magnetic fluxes $\boldsymbol{p}_e$ and $\boldsymbol{p}_s$ will remain constant. This situation is analogous to a system of purely inductive closed loops. More specially $\boldsymbol{V}_e=0,\ \boldsymbol{\Omega}_e=0$ implies constancy of the magnetic flux associated with the plasma model. These assumptions result in the well-known ideal MHD situation, in which lines of constant flux are 'frozen' in the plasma. Since some plasma resistance will occur in practice, the $\boldsymbol{\Omega}_e=0$ assumption is generally false. A distinguishing feature of the model we present is the introduction and consideration of resistance terms in the plasma model from the beginning.
- Replacing the generalised coordinates with $-\boldsymbol{p}$ gives an equivalent model, because of the invariance properties of the canonical equations. In the case of a non-resistive plasma, one may use the fluxes associated with the plasma elements as generalised coordinates. Since one cannot express the resistive form of Ohm's law in terms of flux, this necessitates a loss of generality. As a result, plasma models that describe plasma behaviour in terms of plasma flux functions must necessarily neglect plasma resistance effects.
- Also evident from the $\boldsymbol{I}_e$ equation is the necessity of current ramping in $\boldsymbol{I}_s$ to maintain a steady $\boldsymbol{I}_e$ against the plasma resistance, or alternatively a nonzero $\boldsymbol{V}_e$. It can be seen from (12), that in the case of a plasma resistance, a constant $\boldsymbol{V}_s$ will not suffice to maintain a steady plasma current and position. As such, the plasma resistance is an important feature of the model. This conclusion is illustrated by a simple, intuitive example in Appendix .
- It is interesting to note that as the plasma mass approaches zero, the plasma profile adjusts to the fields instantaneously. This is the approximation of instantaneous MHD equilibrium.

D. Definitions of plasma bulk properties

A lumped-parameter model can be defined from equations (11) to (14), by defining various averaged plasma quantities. The total plasma current will be called I_p. The equilibrium plasma current density distribution $j(R,\ z)$ is calculated from the Grad-Shafranov equation [1], [2] by an inverse equilibrium reconstruction code. We take the plasma mass to be zero, because the inertial forces are tiny compared to the other forces experienced by the plasma.

The average plasma radial position R is defined by a current-weighted average of plasma element radial positions [16],

$$R=\frac{\sum_k i_k R_k}{\sum_k i_k}, \qquad (15)$$

The average plasma vertical position z is defined similarly.

The effective mutual inductance matrix between the plasma and structure $\mathbf{M}_{ps}$ is

$$I_p\mathbf{M}_{ps}\boldsymbol{I}_s=\sum_k i_k\mathbf{M}_{ks}\boldsymbol{I}_s \qquad (16)$$

where $\mathbf{M}_{ks}$ is the mutual inductance between the kth plasma element and the vector of structure element currents.

We define the effective plasma self inductance L_p via the equivalent energy of the total current distribution;

$$\frac{1}{2}L_pI_p^2=\frac{1}{2}\sum_k\sum_h i_kM_{kh}i_h \qquad (17)$$

where M_{kh} is the mutual inductance between the hth and kth elements, for $h\neq k$. In the case of $h=k$, the self inductance of the kth element is used.

A lumped-parameter model can be defined from equations (11) to (14), by defining various averaged plasma quantities. The total plasma current will be called I_p. The equilibrium plasma current density distribution $j(R,\ z)$ is calculated from the Grad-Shafranov equation [2], [1] by an inverse equilibrium reconstruction code. We take the plasma mass to be zero, because the associated modes would operate on a frequency much higher than the range of interest.

The average plasma radial position R is defined by a current-weighted average of plasma element radial positions [16],

$$R=\frac{\sum_k i_k R_k}{\sum_k i_k}, \qquad (18)$$

The average plasma vertical position z is defined similarly.

The effective mutual inductance matrix between the plasma and structure $\mathbf{M}_{ps}$ is

$$I_p\mathbf{M}_{ps}\boldsymbol{I}_s=\sum_k i_k\mathbf{M}_{ks}\boldsymbol{I}_s \qquad (19)$$

where $\mathbf{M}_{ks}$ is the mutual inductance between the kth plasma element and the vector of structure element currents.

We define the effective plasma self inductance L_p via the equivalent energy of the total current distribution;

$$\frac{1}{2}L_p I_p^2 = \frac{1}{2}\sum_k \sum_h i_k M_{kh} i_h \tag{20}$$

where M_{kh} is the mutual inductance between the hth and kth elements, for $h \neq k$. In the case of $h = k$, the self inductance of the kth element is used.

To evaluate the internal energy of the plasma, W, we may start with the equations governing the plasma profile:

$$\bigtriangledown p = \boldsymbol{j} \times \boldsymbol{B}$$
$$\mu_0 \boldsymbol{j} = \bigtriangledown \times \boldsymbol{B}.$$

By substitution we have

$$\mu_0 \bigtriangledown p = (\bigtriangledown \times \boldsymbol{B}) \times \boldsymbol{B}.$$

Using the identity

$$(\bigtriangledown \times \boldsymbol{A}) \times \boldsymbol{A} = (\boldsymbol{A}.\bigtriangledown)\boldsymbol{A} - \frac{1}{2}\bigtriangledown \boldsymbol{A}^2$$

gives

$$\mu_0 \bigtriangledown p = (\boldsymbol{B}.\bigtriangledown)\boldsymbol{B} - \frac{1}{2}\bigtriangledown \boldsymbol{B}^2$$
$$\Rightarrow \quad \bigtriangledown \left(p + \frac{\boldsymbol{B}^2}{2\mu_0} \right) = (\boldsymbol{B}.\bigtriangledown)\boldsymbol{B}.$$

At equilibrium and for our geometry the right hand side is small (zero for the circular, small aspect ratio approximation), which gives

$$p + \frac{\boldsymbol{B}^2}{2\mu_0} = const. = \frac{\boldsymbol{B}_0^2}{2\mu_0}$$

where $\boldsymbol{B}_0$ is the magnetic field outside the plasma (where $p = 0$).

We define

$$\beta = \frac{p}{\left(\frac{\boldsymbol{B}^2}{2\mu_0}\right)}.$$

Since W is the energy associated with the pressure, and taking the plasma volume V as $V = 2\pi RS$ where S is the plasma cross-sectional area, we have for W

$$W = pV = \frac{\boldsymbol{B}^2}{2\mu_0}\beta S 2\pi R.$$

We can write

$$W = pV = \int p \, \mathrm{d}S \; 2\pi R.$$

Defining an average poloidal field as $\bar{\boldsymbol{B}}_\theta = \frac{\mu_0 I_p}{l}$, gives a correspondingly averaged poloidal beta,

$$\beta_p = \frac{\int p \, \mathrm{d}S}{S} \frac{2\mu_0}{\bar{\boldsymbol{B}}_\theta^2}.$$

We can then approximate W as

$$W = \frac{\bar{\boldsymbol{B}}_\theta^2}{2\mu_0}\beta_p S 2\pi R.$$
$$= \mu_0 \pi \frac{S}{l^2}\beta_p R I_p^2.$$

The proper evaluation of W requires careful consideration. For comparison, a slightly different treatment is to be found in [8].

E. Linearisation of equations

Equations (11) to (14) define the evolution of the variables $(R, z, I_p, \boldsymbol{I}_s)$. For consistency with earlier work [6], we will replace the variables $(R,\ z)$ with $(RI_p^0,\ zI_p^0)$ in which I_p^0 is the constant equilibrium plasma current. With this change of variable in place, we introduce the perturbations;

$$\boldsymbol{x} = \begin{bmatrix} \boldsymbol{I}_s - \boldsymbol{I}_s^0 \\ (z - z^0)I_p^0 \\ (R - R^0)I_p^0 \\ I_p - I_p^0 \end{bmatrix} = \begin{bmatrix} \delta \boldsymbol{I}_s \\ \delta z I_p^0 \\ \delta R I_p^0 \\ \delta I_p \end{bmatrix}. \tag{21}$$

The four physics equations are therefore linearised in $\boldsymbol{x}$ about the tokamak equilibrium $\boldsymbol{x}^0 = \boldsymbol{0}$, to give four linear equations. These linear matrices can then be cast in the standard state-space model form

$$\dot{\boldsymbol{x}} = \mathbf{A}\boldsymbol{x} + \mathbf{B}\boldsymbol{u}$$
$$\boldsymbol{y} = \mathbf{C}\boldsymbol{x} + \mathbf{D}\boldsymbol{u}. \tag{22}$$

The linearised structure circuit equation, plasma circuit equation and plasma force balance equations can be represented as follows;

$$\begin{bmatrix} \mathbf{L}_s & \left.\frac{\partial \mathbf{M}_{sp}}{\partial z}\right|_0 & \cdots \\ \left.\frac{\partial \mathbf{M}_{ps}}{\partial z}\right|_0 & \left(\frac{1}{2}\left.\frac{\partial^2 L_p}{\partial z^2}\right|_0 + \left.\frac{\partial^2 \mathbf{M}_{ps}}{\partial z^2}\right|_0 \frac{\boldsymbol{I}_s^0}{I_p^0}\right) & \cdots \\ \left.\frac{\partial \mathbf{M}_{ps}}{\partial R}\right|_0 & \left(\frac{1}{2}\left.\frac{\partial^2 L_p}{\partial z \partial R}\right|_0 + \left.\frac{\partial^2 \mathbf{M}_{ps}}{\partial z \partial R}\right|_0 \frac{\boldsymbol{I}_s^0}{I_p^0}\right) & \cdots \\ \mathbf{M}_{ps}^0 & \left.\frac{\partial L_p}{\partial z}\right|_0 & \cdots \end{bmatrix}$$
$$\begin{matrix} \cdots & \left.\frac{\partial \mathbf{M}_{sp}}{\partial R}\right|_0 & \cdots \\ \cdots & \left(\frac{1}{2}\left.\frac{\partial^2 L_p}{\partial z \partial R}\right|_0 + \left.\frac{\partial^2 \mathbf{M}_{ps}}{\partial z \partial R}\right|_0 \frac{\boldsymbol{I}_s^0}{I_p^0}\right) & \cdots \\ \cdots & \left(\frac{1}{2}\left.\frac{\partial^2 L_p}{\partial R^2}\right|_0 + \left.\frac{\partial^2 \mathbf{M}_{ps}}{\partial R^2}\right|_0 \frac{\boldsymbol{I}_s^0}{I_p^0}\right) & \cdots \\ \cdots & \left(\left.\frac{\partial \mathbf{M}_{ps}}{\partial R}\right|_0 \frac{\boldsymbol{I}_s^0}{I_p^0} + \left.\frac{\partial L_p}{\partial R}\right|_0 + \mu_0 \frac{2\pi S}{l^2}\beta_p\right) & \cdots \end{matrix}$$
$$\begin{bmatrix} \cdots & \mathbf{M}_{sp}^0 \\ \cdots & \left.\frac{\partial L_p}{\partial z}\right|_0 \\ \cdots & \left(\left.\frac{\partial L_p}{\partial R}\right|_0 + \left.\frac{\partial \mathbf{M}_{ps}}{\partial R}\right|_0 \frac{\boldsymbol{I}_s^0}{I_p^0} + \mu_0 \frac{2\pi S}{l^2}\beta_p\right) \\ \cdots & L_p^0 + \mu_0 \frac{2\pi S}{l^2}\beta_p R^0 \end{bmatrix} \dot{\boldsymbol{x}}$$
$$+ \begin{bmatrix} \boldsymbol{\Omega_s} & 0 & 0 & 0 \\ \boldsymbol{0} & 0 & 0 & 0 \\ \boldsymbol{0} & 0 & 0 & 0 \\ \boldsymbol{0} & 0 & 0 & \Omega_p \end{bmatrix} \boldsymbol{x} = \begin{bmatrix} \mathbf{I} & 0 \\ \boldsymbol{0} & 0 \\ \boldsymbol{0} & 0 \\ \boldsymbol{0} & I \end{bmatrix} \begin{bmatrix} \delta \mathbf{V}_s \\ \delta V_p \end{bmatrix}. \tag{23}$$

This is of the form $\mathcal{M}\dot{\boldsymbol{x}} + \mathcal{R}\boldsymbol{x} = \boldsymbol{u}$. Comparing (23) with (22) gives the matrix of coefficients $\mathbf{A}$, and the control matrix $\mathbf{B}$;

$$\mathbf{A} = -\mathcal{M}^{-1}\mathcal{R}$$
$$\mathbf{B} = \mathcal{M}^{-1} \begin{bmatrix} \mathbf{I} & \boldsymbol{0} & \boldsymbol{0} & \boldsymbol{0} \\ 0 & 0 & 0 & I \end{bmatrix}^T.$$

Note that $\mathcal{M}$ and $\mathcal{R}$ are symmetric with $\mathcal{M}$ positive definite and $\mathcal{R}$ positive semi-definite.

From a minimal set of assumptions we have derived a linear, time invariant model in state-space form. All linearised tokamak models making similar assumptions can be expressed in this structural form. Within this framework we can derive all models that represent axisymmetric perturbations about given MHD equilibria.

F. The RZIP linear model

Further to the assumptions detailed earlier, the linear RZIP model also makes the rigid current displacement assumption, namely that the normalised current profile is independent of movements in the R and z directions and of changes in plasma current. It follows therefore that changes in the plasma current profile are not modelled. As such, $\left.\frac{\partial L_p}{\partial z}\right|_0 = 0$.

Changes to the current and pressure profile can be approximately modelled by permitting perturbations to β_p. These changes are then introduced as disturbances in $\dot{\beta}_p$ on the right hand side of (23), as in [8].

The rigid current displacement assumption allows us to calculate the plasma mutual and self inductance derivatives simply and directly.

For example, the mutual inductance between two plasma elements must satisfy:

$$\frac{\partial M_{fg}}{\partial R} = \frac{\partial M_{fg}}{\partial R_f}\frac{\partial R_f}{\partial R} + \frac{\partial M_{fg}}{\partial R_g}\frac{\partial R_g}{\partial R}.$$

The rigid current displacement assumption fixes the two radius relations as

$$\frac{\partial R_f}{\partial R} = \frac{\partial R_g}{\partial R} = 1.$$

III. The control problem

The remainder of the paper is concerned with the design and evaluation of a control system for the TCV tokamak [14]. We will use the linearised model described in Section II as a basis for designing this controller. It will be tested on a nonlinear code based on a sequence of Grad-Shafranov equilibria [17].

A. Control objectives

The primary interest of this work is the study of control systems for elongated plasmas in TCV. As with all elongated plasmas, the equilibrium under consideration is unstable in the vertical position and so the open-loop plant is characterised by a single unstable pole that requires stabilisation. One of the major challenges is the uncertainty in the modelling of the tokamak plasma dynamics together with the fact that these dynamics vary with the operating conditions. For this reason, it is important that the proposed control system has adequate robust stability and performance margins. We will also seek to decouple the five outputs that characterise the plasma shape, position and current. Ideally, we would like to be able to implement variation in any one of these outputs without influencing the others.

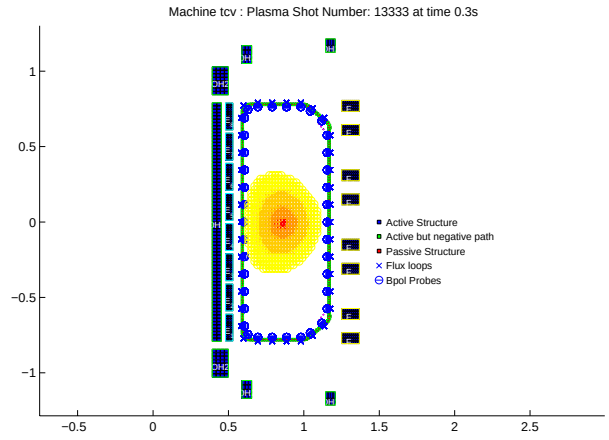

Fig. 4. TCV equilibrium 13333

B. The RZIP model of TCV

The RZIP model plus power supplies has been qualified against the TCV equilibrium 13333 [6]. The plasma in this shot is well understood and unstable with a moderate growth rate measured and predicted by RZIP as approximately $100s^{-1}$; the equilibrium profile is shown in Figure 4. The five control parameters used for controlling this type of equilibrium on TCV are:

- p_{vert}, the radial flux imbalance (a radial position measurement);
- tri_{out}, the outboard field curvature;
- tri_{in}, the inboard field curvature;
- zI_p, the product of plasma vertical position and current;
- I_p, the plasma current.

The particular RZIP model used for controller design assumes a superconducting plasma (see Section II). This choice is made because the controller will be tested on the ideal MHD code PROTEUS, which makes a similar assumption. Figure 5 shows the singular value plot of the TCV RZIP model which has 18 inputs and 5 outputs. It can be seen from this figure that there is a large spread in the singular value magnitudes. As is standard practice, we will seek to reduce the transfer function's condition number by scaling. Indeed, this will be the initial step of a loop-shaping based design.

A characterising feature of models based on ideal MHD assumptions is the introduction of uncontrollable modes at the origin. The underlying mechanism that gives rise to these modes is described briefly in Appendix using simple circuit theoretic arguments. Since these poles cannot exist in reality, we will remove them from the RZIP model using a standard model reduction algorithm [18].

C. Modelling of power supplies

The poloidal field (PF) coil power supplies are approximated by single pole filters, expressed in the state-space form as

$$A = -diag\left(\frac{1}{\tau_c}\right), \quad B = diag\left(\frac{1}{\tau_c}\right), \quad C = I, \quad D = I$$

where $\tau_c = 0.3ms$ for all PF coil power supplies used. Throughout the plant referred to is the tokamak including the power supplies.

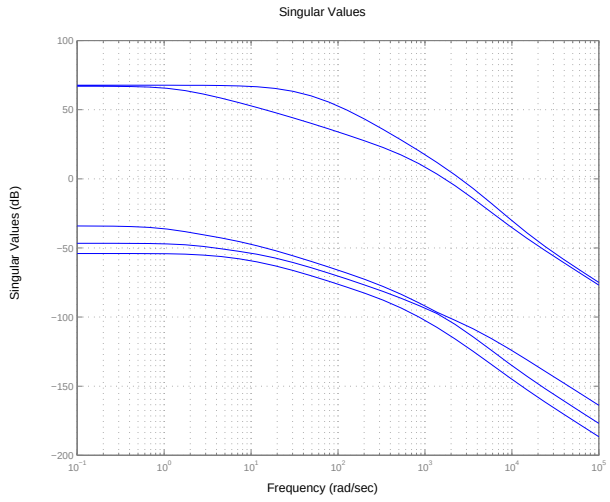

Fig. 5. Singular value plot of TCV RZIP model

IV. Robust controller design

Motivated by its simplicity, we will use the the $\mathcal{H}_\infty$ normalised coprime factorisation method [19], [20] for the controller synthesis. In many respects the research presented here is an evolution of that presented in [21]. After completing the loop shaping and controller synthesis, we will make use of some recent research [13] that facilitates a reduction in the controller order with guaranteed properties.

A. Normalised left coprime factorisation perturbations

A set of plant models that will be used to represent the machine will be characterised in terms if a perturbed normalised coprime factorisation. We suppose that $\mathbf{G}$ is the nominal plant model. Then

$$\mathbf{G} = \mathbf{M}^{-1}\mathbf{N} \tag{24}$$

is a normalised left coprime factorisation of $\mathbf{G}$ if $\mathbf{M}, \mathbf{N} \in \mathcal{H}_\infty$ are coprime and satisfy

$$\mathbf{M}\mathbf{M}' + \mathbf{N}\mathbf{N}' = \mathbf{I}.$$

Given such a factorisation we define the model set

$$\mathcal{G}_\gamma = \left\{ (\mathbf{M}-\mathbf{\Delta}_M)^{-1}(\mathbf{N}+\mathbf{\Delta}_N) : \begin{array}{l} [\mathbf{\Delta}_N \ \ \mathbf{\Delta}_M] \in \mathcal{H}_\infty \\ \|[\mathbf{\Delta}_N \ \ \mathbf{\Delta}_M]\|_\infty < \gamma^{-1} \end{array} \right\}. \tag{25}$$

B. The optimisation problem

Our aim is to design a controller that is optimal in the sense of minimising γ, in order to maximise the size of admissible perturbations (by (25)). From Figure 6 we see that

$$\begin{bmatrix} u \\ y \end{bmatrix} = \mathcal{H}(\mathbf{G}, \mathbf{K})\phi, \qquad \phi = [\mathbf{\Delta}_N \ \ \mathbf{\Delta}_M] \begin{bmatrix} u \\ y \end{bmatrix},$$

where

$$\mathcal{H}(\mathbf{G}, \mathbf{K}) = \begin{bmatrix} \mathbf{K} \\ \mathbf{I} \end{bmatrix} (\mathbf{I} - \mathbf{G}\mathbf{K})^{-1}\mathbf{M}^{-1}. \tag{26}$$

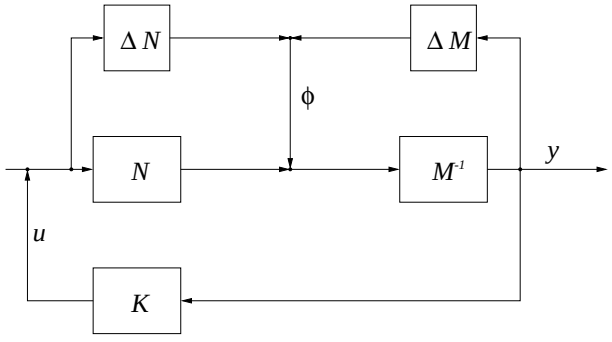

Fig. 6. Robust controller design problem

From the small gain theorem [19], the condition

$$\|\mathcal{H}(\mathbf{G}, \mathbf{K})\|_\infty \leq \gamma \tag{27}$$

will ensure that the closed loop will be stable for all plants in the model set $\mathcal{G}_\gamma$. To maximise the robustness of the closed loop, we require a controller that minimises γ.

C. Parameterisation of all suboptimal controllers

The following result gives a parameterisation of all suboptimal controllers.

Lemma IV.1: [13], [19], [20], [22] Let $\mathbf{G}$ have a minimal realisation $\mathbf{G} \stackrel{s}{=} (A, B, C, 0)$. Then there exist unique stabilising and positive definite solutions X, Y to the algebraic Riccati equations

$$A'X + XA - XBB'X + C'C = 0 \tag{28}$$

$$AY + YA' - YC'CY + BB' = 0 \tag{29}$$

respectively, and

$$\gamma_{opt} = \sqrt{1 + \lambda_{max}(XY)} \geq 1. \tag{30}$$

For any $\gamma > \gamma_{opt} \geq 1$ let $\beta = \sqrt{1-\gamma^{-2}}$ so that $0 < \beta \leq 1$ and define $Z = \left(I - \gamma^{-2}\beta^{-2}XY\right)^{-1}$. Then all suboptimal controllers are given by the parametrisation

$$\begin{array}{c} \mathbf{K} = (\mathbf{\Theta}_{11}\mathbf{Q} + \mathbf{\Theta}_{12})(\mathbf{\Theta}_{21}\mathbf{Q} + \mathbf{\Theta}_{22})^{-1}, \\ \mathbf{Q} \in \mathcal{RH}_\infty, \quad \|\mathbf{Q}\|_\infty < \gamma, \end{array} \tag{31}$$

where

$$\mathbf{\Theta} = \begin{bmatrix} \mathbf{\Theta}_{11} & \mathbf{\Theta}_{12} \\ \mathbf{\Theta}_{21} & \mathbf{\Theta}_{22} \end{bmatrix} \stackrel{s}{=} \left[\begin{array}{c|cc} A - BB'X & ZB & \beta^{-1}ZYC' \\ \hline -\beta^{-2}B'X & I & 0 \\ \beta^{-2}C & 0 & \beta^{-1}I \end{array}\right] \in \mathcal{RH}_\infty. \tag{32}$$

We will also require

$$\mathbf{\Theta}^{-1} \stackrel{s}{=} \left[\begin{array}{c|cc} Z(A - YC'C)Z^{-1} & ZB & ZYC' \\ \hline \beta^{-2}B'X & I & 0 \\ -\beta^{-1}C & 0 & \beta I \end{array}\right] \in \mathcal{RH}_\infty \tag{33}$$

in the sequel.

Remark IV.1: Taking $\mathbf{Q} = 0$ in (31) gives the central controller in the form of a right coprime factorisation

$$\mathbf{K}_{11} = \mathbf{\Theta}_{12}\mathbf{\Theta}_{22}^{-1} \stackrel{s}{=} \left[\begin{array}{c|c} A - BB'X - \beta^{-2}ZYC'C & ZYC' \\ \hline -\beta^{-2}B'X & 0 \end{array}\right]. \tag{34}$$

We will use this controller throughout.

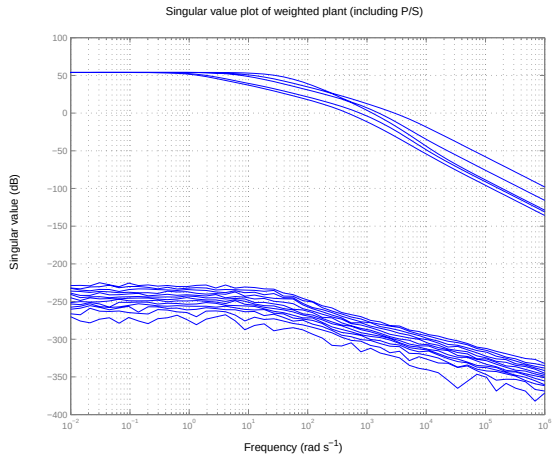

Fig. 7. Response of the weighted plant

D. Choice of weighting matrices

It is evident from Figure 5 that the unweighted plant model has five non-zero singular values spread over more than 100dB at low frequency. As this will lead to highly "direction sensitive" responses, it was deemed necessary to rescale the outputs, thereby balancing the singular values. To do this, we post-multiply $\mathbf{G}$ by

$$\mathbf{W}_o = 500\mathbf{G}^{\#}(0)$$

in which $\mathbf{G}^{\#}(0)$ is a generalised inverse of $\mathbf{G}(0)$, to give

$$\mathbf{G}_W = 500\mathbf{G}^{\#}(0)\mathbf{G}.$$

The singular values of the weighted plant $\mathbf{G}_W$ are shown in Figure 7. As expected, five of the singular values has associated DC gain of 500 (54dB), while the remaining ones are effectively zero. As will be shown, this simple loop shape leads to acceptable closed-loop response when the controller given by (34) is implemented. Clearly the controller must be synthesised from a state-space model of $\mathbf{G}_W$ rather than $\mathbf{G}$.

V. Normalised $\mathcal{H}_\infty$ controller reduction

It follows from (34) that the degree of the controller is the same as that of the plant. In our case, the plant's McMillan degree is 76 and this would lead to a correspondingly high order controller.

In this section, we apply the relative error controller order reduction procedure given in [13]. In this reference it is shown that the observability Gramian of the realisation of $\mathbf{\Theta}$ in (32), and the controllability Gramian of $\mathbf{\Theta}^{-1}$ in (33), may be expressed in terms of X and Y. These matrices are the unique positive definite solutions of (28) and (29) respectively:

Theorem V.1: [13] Let $P = P' \geq 0$ be the controllability Gramian of the realisation of $\mathbf{\Theta}^{-1}$ in Lemma IV.1 and let $Q = Q' \geq 0$ be the observability Gramian of the realisation of $\mathbf{\Theta}$ in Lemma IV.1 so that

$$[Z(A-YC'C)Z^{-1}]P+P[Z(A-YC'C)Z^{-1}]'+ZBB'Z'+ZYC'CYZ'=0$$

$$(A-BB'X)'Q+Q(A-BB'X)+\beta^{-4}XBB'X+\beta^{-4}C'C=0.$$

Then $P = ZYZ'$ and $Q = \beta^{-4}X$.

Suppose that the realisation of $\mathbf{\Theta}$ is inverse-weighted balanced, so that

$$P = Q = \mathrm{diag}(\Sigma_1, \Sigma_2) \tag{35}$$

where,

$$\Sigma_1 = \mathrm{diag}(\sigma_1 I_{s_1}, \ldots, \sigma_r I_{s_r}), \Sigma_2 = \mathrm{diag}(\sigma_{r+1} I_{s_{r+1}}, \ldots, \sigma_N I_{s_N})$$

with $\sigma_1 > \cdots \sigma_N \geq 0$ and that the realisation in (32) is partitioned compatibly with Σ_1 and Σ_2:

$$\mathbf{\Theta} \stackrel{s}{=} \left[\begin{array}{cc|c} A_{11} & A_{12} & B_1 \\ A_{21} & A_{22} & B_2 \\ \hline C_1 & C_2 & D_{\mathbf{\Theta}} \end{array}\right] \tag{36}$$

where $D_{\mathbf{\Theta}} = \begin{bmatrix} I & 0 \\ 0 & \beta I \end{bmatrix}$. Then

$$\hat{\mathbf{\Theta}} = \left[\begin{array}{cc} \hat{\mathbf{\Theta}}_{11} & \hat{\mathbf{\Theta}}_{12} \\ \hat{\mathbf{\Theta}}_{21} & \hat{\mathbf{\Theta}}_{22} \end{array}\right] \stackrel{s}{=} \left[\begin{array}{c|c} A_{11} & B_1 \\ \hline C_1 & D_{\mathbf{\Theta}} \end{array}\right] \tag{37}$$

is stable and minimum phase and $\hat{\mathbf{\Theta}} = (\mathbf{I} + \mathbf{\Delta})\mathbf{\Theta}$, where $\mathbf{\Delta} \in \mathcal{RH}_\infty$ satisfies $\|\mathbf{\Delta}\|_\infty \leq \delta$ where [19]

$$\delta := -1 + \prod_{i=r+1}^{N} (1 + 2\sigma_i\sqrt{1+\sigma_i^2} + 2\sigma_i^2) \tag{38}$$

and

$$\sigma_i^2 = \frac{\nu_i^2}{\beta^4}\left(1 - \frac{\nu_i^2}{\gamma^2\beta^2}\right)^{-2}.$$

The quantities $\nu_1^2, \ldots, \nu_N^2$ are the (distinct) eigenvalues of XY.

Since the central controller is obtained from the controller generator in the form of the right coprime factorisation (34), it is shown in [13] that the approximation of $\mathbf{\Theta}$ induces a relative reduction on the coprime factors of the normalised central controller. Combined with the bound on the relative approximation error, this gives guaranteed *a priori* bounds on closed-loop stability and performance degradation and provides an intimate link between the controller synthesis and controller reduction problems. These results are summarised in the following theorem:

Theorem V.2: [13] Let $\mathbf{K}_{11} = \mathbf{\Theta}_{12}\mathbf{\Theta}_{22}^{-1}$ be the central controller defined in (34). Suppose that T is an inverse-weighted balancing transformation for $\mathbf{\Theta}$ so that

$$\begin{aligned} \Sigma &= T^{-1}(ZYZ')(T^{-1})' = T'(\beta^{-4}X)T \\ &= \mathrm{diag}(\sigma_1 I_{s_1}, \ldots, \sigma_r I_{s_r}, \sigma_{r+1} I_{s_{r+1}}, \ldots, \sigma_N I_{s_N}) \\ &= \mathrm{diag}(\Sigma_1, \Sigma_2) \end{aligned}$$

with $\sigma_1 > \ldots > \sigma_N \geq 0$. Apply the similarity transformation T to the central controller $\mathbf{K}_{11}$ and partition compatibly with Σ_1 and Σ_2

$$\mathbf{K}_{11} \stackrel{s}{=} \left[\begin{array}{c|c} T^{-1}(A - BB'X - \beta^{-2}ZYC'C)T & T^{-1}(ZYC') \\ \hline (-\beta^{-2}B'X)T & 0 \end{array}\right]$$

$$\stackrel{s}{=:} \left[\begin{array}{cc|c} \hat{A}_{11} & \hat{A}_{12} & \hat{B}_1 \\ \hat{A}_{21} & \hat{A}_{22} & \hat{B}_2 \\ \hline \hat{C}_1 & \hat{C}_2 & 0 \end{array}\right].$$

Define the reduced order controller

$$\hat{\mathbf{K}} := \hat{\mathbf{\Theta}}_{12}\hat{\mathbf{\Theta}}_{22}^{-1} \stackrel{s}{=} \left[\begin{array}{c|c} \hat{A}_{11} & \hat{B}_1 \\ \hline \hat{C}_1 & 0 \end{array}\right]. \tag{39}$$

Then $\mathcal{H}(\mathbf{G}_W, \hat{\mathbf{K}})$ is stable if $\gamma\delta < 1$, in which case

$$\|\mathcal{H}(\mathbf{G}_W, \hat{\mathbf{K}})\|_\infty < \frac{\gamma}{1-\delta\gamma}.$$

VI. Controller Reduction and Implementation

The final phase of the work is aimed at the implementation and testing of the reduced-order controller described in Theorem V.2.

Preliminary testing was conducted on the linear RZIP model. Once the tests were deemed satisfactory, more demanding simulations were performed on the nonlinear PROTEUS model [17].

This programme began with the synthesis of a full-order normalised coprime factor controller. The synthesis used the formula (34) and a sub-optimal $\gamma = 3.02$. The controller realisation was then balanced in accordance with Theorem V.2 so that reduced order controllers can be 'read off'. This sequence of reduced order controllers was combined with $\mathbf{G}_W$ in order to generate the plot shown in Figure 8. This diagram shows, for each reduced order controller, the infinity norm of the closed-loop transfer function as well as the upper bound given in (38). It is clear from this diagram that the closed-loop performance improves very little for controllers of McMillan degree ≥ 16. The upper bound is clearly conservative and indicates that a controller of degree ≥ 30 is required. It should also be noted that the reduces-order controllers are stabilising for order ≥ 12, while the bounds in Theorem V.2 indicate that this lowest order for stability is 27.

On the basis of the data in Figure 8, a controller of order 18 was selected; this represents a significant reduction from the full order of 76.

Figures 9 and 10 show the effect of the reduction process on the controller and closed-loop transfer functions respectively. Figure 9 shows that the controller reduction from 76 to 18 states has almost no effect on its transfer function. Figure 10 shows that the controller reduction process increases the closed-loop infinity norm from $\gamma = 3.02$ to $\gamma = 3.91$. Interestingly, the almost imperceptible changes made by the reduction process to the controller singular values have a far more pronounced impact on the closed-loop.

VII. Controller Simulation Testing

Even on a relatively small tokamak such as TCV, experimental time and machine failures are potentially expensive. In order to obviate these difficulties, we undertook a programme of controller testing at a simulation level prior to any hardware implementation. The two steps involved simulation testing on RZIP, with a second programme of tests on PROTEUS. The outcome of the simulation tests will now be presented.

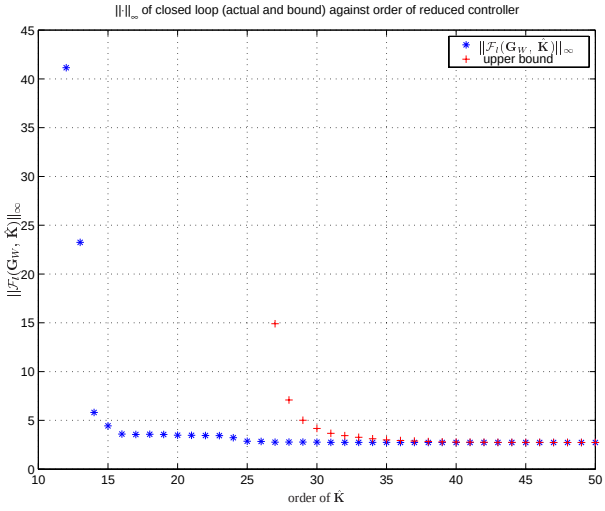

Fig. 8. Plot of $||\mathcal{F}_l(\mathbf{G}_W, \hat{\mathbf{K}})||_\infty$ (*) against the order of the reduced controller. The closed-loop is unstable for controllers of order less than 12. The *a priori* bound on $||\mathcal{F}_l(\mathbf{G}_W, \hat{\mathbf{K}})||_\infty$ is shown as a (+) where stability is *a priori* guaranteed.

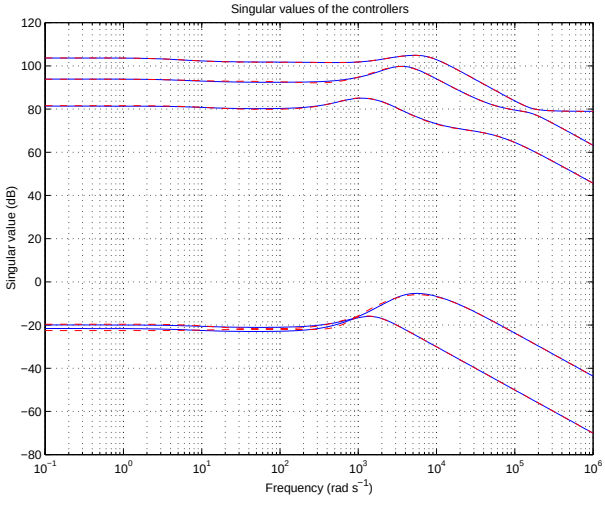

Fig. 9. Singular value plots of the (-) $\gamma = 3.02$ controller, (- -) reduced $\gamma = 3.91$ controller (18 states)

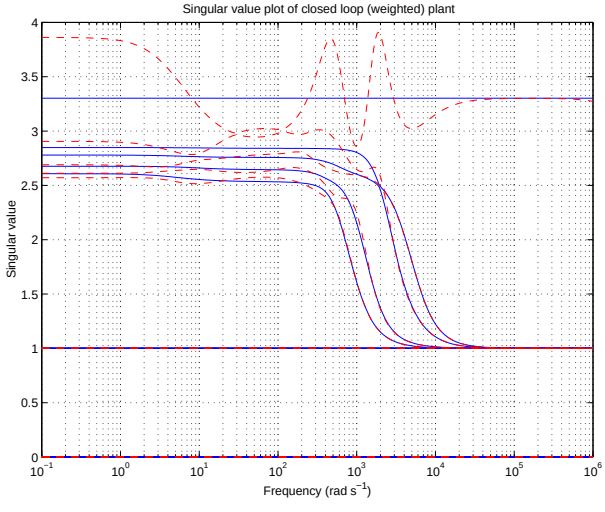

Fig. 10. Singular value plot for the weighted closed-loop plant with (-) $\gamma = 3.02$ and (- -) reduced $\gamma = 3.91$ controller

A. *Testing on RZIP in SIMULINK*

Since RZIP models are linear, the only source of nonlinearity in these simulations will be power supply saturation. It is convenient to use the SIMULINK environment to introduce these effects. A full list of the power supply limits is given in the table below [14].

PF coil P/S	Saturation voltage (+/-)	Saturation current (+/-)
OH1, OH2	1399V	31kA
E1-E8	648V	7.7kA
F1-F8	1250V	7.7kA
G	566V	500A (continuous)
		2000A ($2s$ /$5min$)

For the purposes of this study, we designed a controller that combines good robust stability margins, speed of response, dynamic tracking characteristics and closed-loop decoupling. In order to test for these various characteristics, we drove the closed-loop system with a vector valued reference signal that comprised pulse functions that were staggered in time. The pulse amplitudes were chosen to represent 'reasonable', but demanding excursions given the machine dimensions [5]. The temporal separation between the pulses allowed us to examine the inter-loop cross-coupling. The performance of the 18-state reduced order controller is shown in Figure 11. This diagram also shows the response of the existing PID controller, which is currently implemented on TCV. It is clear from the responses that the controller possesses all the desired properties; the pulse inputs lie underneath the responses and are barely visible on the plot. This is testimony to the controller's excellent tracking properties. It is also clear that the only cross-coupling appears at the pulse edges. In comparison, the existing PID controller shows inconsistent behavior with some loops under-damped, while others are comparatively sluggish. The PID control also has inferior decoupling properties.

Although saturation limits were included in the simulation, these played very little role in the particular responses shown here. This is because the TCV power supplies were deliberately over-designed to increase the machine's research flexibility.

B. *Testing on the PROTEUS nonlinear tokamak simulation code*

PROTEUS is a tried and tested nonlinear tokamak simulation code that solves the Grad-Shafranov equation using an iterative finite element method. As such it can be used to predict the tokamak plasma's evolution forwards in time, under the assumption of a fixed plasma current. In order to initialise these simulations, PROTEUS requires data about the initial equilibrium, specifically the coil currents and some plasma profile parameters.

Although PROTEUS can model temporal changes in the plasma shape, it does not take account of transport and resistivity phenomena that are known to occur. Since the original code does not have a plasma circuit equation, one had to be introduced, although this is not strictly self-consistent with the

[5] This includes both the machine geometry and the electromagnetic specifications.

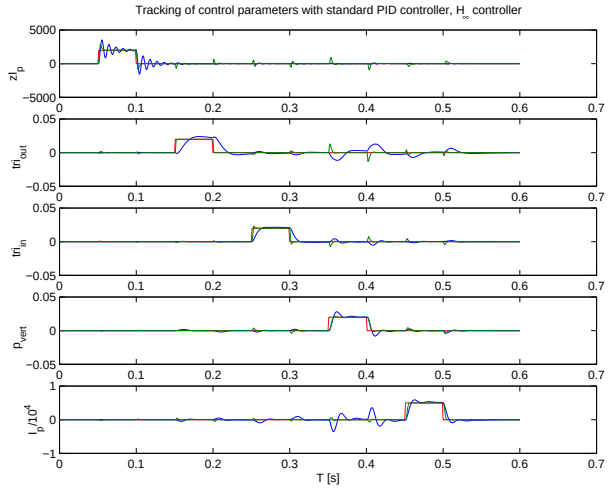

Fig. 11. Results of closed-loop simulation showing (-) reference, (-) PID and (-) RZIP simulated response.

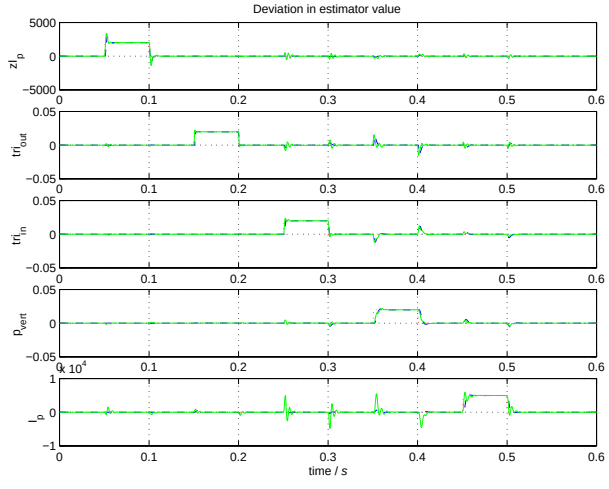

Fig. 12. Results of closed loop simulations, showing (-) the PROTEUS simulated response, (:) the reference and (- -) the RZIP simulated response.

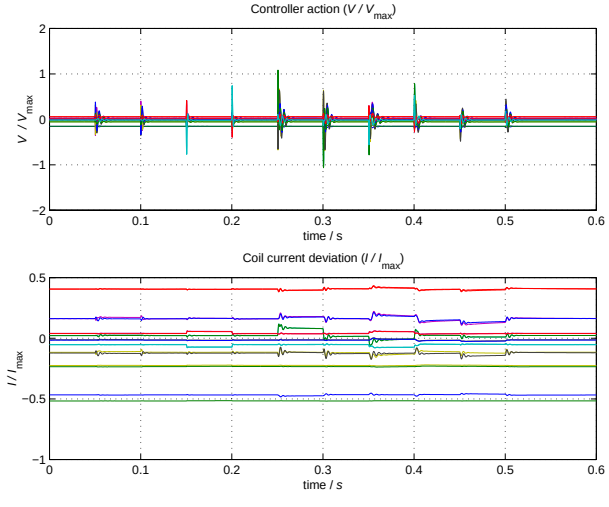

Fig. 13. Closed loop simulation coil voltage and current.

initial assumptions. The controller acts to change the plasma current so this dynamic response must be represented.

In order to complete the simulation work presented here, we had to introduce a facility for modelling discrete-time controllers and estimator matrices that generate the controlled plant outputs.

The issue of delays introduced by discretisation of the feedback controllers has been addressed in [11], in which a high-order $\mathcal{H}_\infty$ controller was tested on the TCV tokamak. The continuous-time controller used here was discretised using a 0.1ms sampling period, prior to testing on PROTEUS. The TCV diagnostics and computer system are capable of supporting this sampling frequency.

The PROTEUS simulations represent a form of robustness test, because the code is very different to the RZIP model used in the controller synthesis. The successful operation of the PROTEUS closed-loop therefore lends confidence to the idea that the controller will work successfully on the hardware system.

Figure 12 shows the results of the PROTEUS simulation with a $0.1ms$ time step. To aid comparison, the RZIP results are also shown on the same diagram. The input and nominal equilibrium conditions were chosen to match those associated with the RZIP results. It can be seen from Figure 12 that there is good agreement between the PROTEUS and the RZIP predictions. With that said, one can see a number of lightly damped resonances in the PROTEUS plasma current that are absent in the RZIP equivalent. This is considered likely to represent the inconsistencies in the PROTEUS modelling of the plasma circuit equation.

The practical import of this close agreement is that RZIP simulations that require a few minutes to compute can be used instead of PROTEUS predictions that require days on a like-for-like basis.

Figure 13 shows the coil voltage and current as a fraction of the saturation limits. This diagram shows that the power supplies do not saturate except very briefly at 0.25 and 0.3 seconds where the inner triangularity is stimulated. This does not lead to a loss of control in the simulation. Since the slight saturation occurs only when the inner triangularity is stimulated hard, and this parameter is unlikely to be pulsed in normal TCV operation, the saturation is unlikely to lead to a loss of plasma control on TCV.

VIII. Discussion

We have presented a new modelling and control system design paradigm for tokamak fusion reactors. From the initial modelling assumptions, the methodology takes us through the modelling process to low-order controllers with good performance and robustness characteristics.

Starting with clearly stated assumptions, a nonlinear model together with its linearised counterpart are derived using known techniques from Hamiltonian mechanics. This approach to the modelling problem clarifies many of the relationships between the assumptions and the model properties. For example, it becomes clear that current ramping is necessary to maintain the plasma current when the plasma resistance is nonzero. Since future machines will operate on longer time-scales, plasma resistance effects will become more important. The model presented here incorporates plasma resistance thereby satisfying this need. The effect of removing plasma resistance from the model is also clarified. We show that this leads to the introduction of uncontrollable modes at the origin. This is examined further in the appendix.

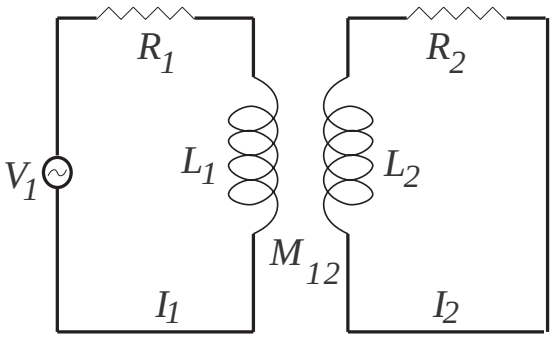

Fig. 14. A coupled LR circuit

The second part of the paper demonstrates the effectiveness of a novel model reduction methodology for normalised coprime factor controller reduction. The known procedures of normalised coprime factor controller design produce control systems with order equal to that of the loop-shaped plant [19], [23]. Since we have used non-dynamic weights, the controller order is 76 according to this established wisdom. We have demonstrated that it is possible to reduce the controller order to 18 using the techniques described in [13] without a significant performance degradation. It was also demonstrated that this performance was successfully transferred to the nonlinear tokamak simulation code PROTEUS. In this context, this successful transfer is indicative of the inherent robustness properties of the controller. This is because PROTEUS is based on modelling assumptions quite different to those used in the model presented here, on which the controller synthesis was based. Given the successful transfer to PROTEUS, we are confident that good performance will be achieved on the TCV hardware using this methodology.

IX. Acknowledgements

The authors would like to thank John Wainwright for the generosity with which he gave his time to help set up PROTEUS, and for lively discussions and ideas about the modelling.

Appendix

The purpose of this appendix is to illustrate, using the simple LR circuit in Figure 14, the mechanism behind the creation of uncontrollable modes in tokamak models containing idealised superconducting plasmas[6]. To the author's knowledge this problem has not been discussed previously.

[6]The results are also relevant to tokamaks with superconducting coils such as ITER. However in that case we would not simply be able to ignore the resulting uncontrollable modes.

In this diagram the secondary circuit represents the plasma, the primary circuit represents the tokamak coils and the mutual inductance the magnetic coupling between them.

It follows from simple circuit theory that:

$$\left[\begin{array}{c} 1 \\ 0 \end{array}\right] V_1 = \left[\begin{array}{cc} L_1 & M_{12} \\ M_{12} & L_2 \end{array}\right] \left[\begin{array}{c} \dot{I}_1 \\ \dot{I}_2 \end{array}\right] + \left[\begin{array}{cc} R_1 & 0 \\ 0 & R_2 \end{array}\right] \left[\begin{array}{c} I_1 \\ I_2 \end{array}\right] \tag{40}$$

which can be put into state-space form:

$$\left[\begin{array}{c} 1 \\ 0 \end{array}\right] u = \mathcal{M}\dot{x} + \mathcal{R}x$$

$$\Rightarrow \quad \dot{x} = -\mathcal{M}^{-1}\mathcal{R}x + \mathcal{M}^{-1}\left[\begin{array}{c} 1 \\ 0 \end{array}\right] u,$$

with

$$A = -\mathcal{M}^{-1}\mathcal{R},$$

and

$$B = \left[\begin{array}{c} \alpha \\ \gamma \end{array}\right]$$

where

$$\mathcal{M}^{-1} = \left[\begin{array}{cc} \alpha & \beta \\ \gamma & \delta \end{array}\right].$$

Observe that $\mathcal{M}$ is necessarily invertible because $L_1 > M_{12}$ and $L_2 > M_{12}$.

Hence

$$A = -\left[\begin{array}{cc} \alpha R_1 & \beta R_2 \\ \gamma R_1 & \delta R_2 \end{array}\right].$$

It follows from standard passivity arguments that $\mathrm{Re}\ \lambda_i(A) < 0$ for $R_1,\ R_2 > 0$.

The controllability matrix is

$$\left[\begin{array}{c|c} sI - A & B \end{array}\right] = \left[\begin{array}{cc|c} s + \alpha R_1 & \beta R_2 & \alpha \\ \gamma R_1 & s + \delta R_2 & \gamma \end{array}\right]. \tag{41}$$

It is therefore the case that (A, B) is controllable if $R_2 > 0$. On the other hand, if $R_2 = 0$, the matrix in (41) will have unit rank at $s = 0$, indicating the presence of an uncontrollable mode there.

In reality we will never face the $R_2 = 0$ situation and so the associated uncontrollable mode may be ignored.

In the case that $R_2 = 0$, it follows that

$$I_2 = -\frac{M_{12}}{L_2} I_1 + C,$$

demonstrating that under these conditions the two loop currents are dependent.

We can also see that

$$\dot{I}_1 = -\frac{I_2 R_2}{M_{12}}$$

in the case that I_2 is constant, which illustrates the need to ramp I_1 in order that I_2 be maintained at a fixed value.

REFERENCES

[1] V. Mukhovatov and V. Shafranov, "Plasma equilibrium in a tokamak," *Nuclear Fusion*, vol. 11, 1971.

[2] J. Wesson, *Tokamaks*. Oxford Science Publications, 1997.

[3] R. Albanese and F. Villone, "The linearized CREATE-L model for the control of current, position and shape in tokamaks," *Nuclear Fusion*, vol. 38, no. 5, 1998.

[4] D. Humphreys and I. Hutchinson, "Axisymmetric magnetic control design in tokamaks using perturbed equilibrium plasma response modelling," *Fusion Technology*, vol. 23, 1993.

[5] D. Humphreys, J. Leuer, and M. Walker, "minimal plasma response models for design of tokamak equilibrium controllers with high dynamic accuracy," *41st Annual Meeting of Division of Plasma Physics, American Physical Society, Seattle, WA, November 15-19*, 1999.

[6] A. Coutlis, I. Bandyopapadhyay, J. Lister, P. Vyas, R. Albanese, D. Limebeer, F. Villone, and J. Wainwright, "Measurement of the open loop plasma equilibrium response in TCV," *Nuclear Fusion*, vol. 35, no. 5, 1999.

[7] F. Hofmann, J.-M. Moret, and D. Ward, "Stability analysis of the vertical position control loop in TCV using rigid and deformable plasma models," *Nuclear Fusion*, vol. 38, no. 12, 1998.

[8] J. Lister, A. Sharma, D. Limebeer, Y. Nakamura, J. Wainwright, and R. Yoshino, "Plasma equilibrium response modelling and validation on JT-60U," *Nuclear Fusion*, vol. 42, 2002.

[9] E. Lazarus, J. Lister, and G. Neilson, "Control of the vertical instability in tokamaks," *Nuclear Fusion*, vol. 30, no. 1, 1990.

[10] P. Vyas, *Plasma vertical position control on COMPASS-D*. PhD thesis, Oxford University, 1996.

[11] M. Ariola, G. Ambrosino, J. Lister, A. Pironti, F. Villone, and P. Vyas, "A modern plasma controller tested on the TCV tokamak," *Fusion Technology*, vol. 36, 1999.

[12] M. Walker, D. Humphreys, and J. Ferron, "Control of plasma poloidal shape and position in the DIII-D tokamak," *Proceedings of the 36th Conference on Decision and Control, San Diego, California USA, December*, 1997.

[13] H. El-Zobaidi, I. Jaimoukha, and D. Limebeer, "Normalized $\mathcal{H}_\infty$ controller reduction with *a priori* bounds," *IEEE Transactions on Automatic Control*, vol. 46, no. 9, 2001.

[14] J. Lister, F. Hofmann, J.-M. Moret, F. Bühlmann, M. Dutch, D. Fasel, A. Favre, P.-F. Isoz, B. Marletaz, P. Marmillod, Y. Martin, A. Perez, and D. Ward, "The control of Tokamak Configuration Variable plasmas," *Fusion Technology*, vol. 32, 1997.

[15] H. Goldstein, *Classical Mechanics (2nd edition)*. Addison-Wesley, 1980.

[16] J. Wainwright, D. Copsey, D. Limebeer, M. Haines, and A. Portone, "Extensions to single filament modelling of a tokamak plasma," *Nuclear Fusion*, vol. 37, no. 12, 1997.

[17] R. Albanese, J. Blum, and O. de Barbieri *12th Conference on Numerical Simulations of Plasmas, San Francisco, CA.*, 1987.

[18] M. Safonov and R. Chiang, "A Schur method for balanced-truncation model-reduction," *IEEE Transactions on Automatic Control*, vol. 34, no. 7, 1989.

[19] M. Green and D. Limebeer, *Linear Robust Control*. Prentice-Hall, 1995.

[20] K. Glover and D. McFarlane, "Robust stabilisation of normalized coprime factor plant descriptions with $\mathcal{H}_\infty$ -bounded uncertainty," *IEEE Transactions on Automatic Control*, vol. 34, no. 8, 1989.

[21] A. Portone, *Modelling and control of tokamak plasmas in fusion devices*. PhD thesis, University of London, 1994.

[22] K. Zhou, "Frequency-weighted $\mathcal{L}_\infty$ norm and optimal Hankel norm model reduction," *IEEE Transactions on Automatic Control*, vol. 40, no. 10, pp. 1687–1699, 1995.

[23] D. McFarlane and K. Glover, "A loop-shaping design procedure using $\mathcal{H}_\infty$ synthesis ," *IEEE Transactions on Automatic Control*, vol. 37, no. 6, 1992.